Probing Red Blood Cell Morphology Using High-Frequency Photoacoustics

Eric M. Strohm,* Elizabeth S. L. Berndl, and Michael C. Kolios
Department of Physics, Ryerson University, Toronto, Ontario, Canada

ABSTRACT A method that can rapidly quantify variations in the morphology of single red blood cells (RBCs) using light and sound is presented. When irradiated with a laser pulse, an RBC absorbs the optical energy and emits an ultrasonic pressure wave called a photoacoustic wave. The power spectrum of the resulting photoacoustic wave contains distinctive features that can be used to identify the RBC size and morphology. When particles 5–10 μm in diameter (such as RBCs) are probed with high-frequency photoacoustics, unique periodically varying minima and maxima occur throughout the photoacoustic signal power spectrum at frequencies >100 MHz. The location and distance between spectral minima scale with the size and morphology of the RBC; these shifts can be used to quantify small changes in the morphology of RBCs. Morphological deviations from the normal biconcave RBC shape are commonly associated with disease or infection. Using a single wide-bandwidth transducer sensitive to frequencies between 100 and 500 MHz, we were able to differentiate healthy RBCs from irregularly shaped RBCs (such as echinocytes, spherocytes, and swollen RBCs) with high confidence using a sample size of just 21 RBCs. As each measurement takes only seconds, these methods could eventually be translated to an automated device for rapid characterization of RBC morphology and deployed in a clinical setting to help diagnose RBC pathology.

INTRODUCTION

Red blood cells (RBCs) have a flexible biconcave disk shape that enables efficient transport of oxygen to the peripheral cells of the body through the narrow and tortuously winding capillary system (1). Disease, infection, genetic disorders, and variations in blood chemistry can alter the RBC shape, reducing its ability to bend and deform (2). Abnormal RBC morphologies can impede or even obstruct the circulation, causing tissue necrosis in severe cases.

Clinical diagnoses of blood disorders use a set of indices to provide information about individual RBC physical characteristics. The average RBC is ~7.8 μm in diameter and 1–2 μm in height and has a 94 μm^3 volume (3). Current automated diagnostic methods use electrical impedance or light-scattering methods to determine the RBC concentration and mean corpuscular volume. In healthy RBCs, the diameter can be inferred from the volume, as these parameters are directly related (4), but this relation may break down for abnormally shaped RBCs. These tools cannot determine the dimensions or shape directly, indicating only whether a sample is outside the accepted guidelines. Because of their limited ability to diagnose pathology, additional testing is required to identify abnormal RBC morphologies such as spherocytes (spherical RBCs) or echinocytes (spherical shape with crenations). Methods to determine the individual RBC shape through blood smears or optical interference methods (5) are laborious and time intensive, prohibiting analysis of large sample sizes.

RBCs contain large amounts of hemoglobin, a molecule capable of binding oxygen. Hemoglobin significantly absorbs visible light, whereas other tissues do not, thus making blood an ideal contrast agent for photoacoustic imaging in vivo (6). After absorbing energy, the particles rapidly increase in temperature and pressure, resulting in a thermoelastic expansion and emission of a photoacoustic wave. These waves can be detected using conventional ultrasound transducers with frequency sensitivities typically between 10 and 40 MHz (7). This effect has been used in vivo for functional imaging (8), photoacoustic tomography (9), the detection of tumors (10), and imaging of vasculature with millimiter-scale resolution (11,12). The photoacoustic effect can be exploited on the microscale using a photoacoustic microscope (13,14). In this system, conventional ultrasound transducers are combined with a highly focused laser to create in vitro and in vivo micrometer-resolution images of vasculature (15), and even of single cells (16). Current photoacoustic microscopes use inexpensive conventional transducers to produce stunning microsized images with excellent contrast; however, they have a limited photoacoustic frequency range of operation.

Our photoacoustic microscope uses transducers with frequencies >100 MHz, with bandwidths in the hundreds of MHz (17). Like other photoacoustic microscopes, it produces images with micrometer resolution (18,19). However, the distinct advantage of this microscope is the broad ultrasound/photoacoustic frequency bandwidth, which can be used for a quantitative analysis of micron-sized particles (20). For any particle in the 1–50 μm size range (such as RBCs), unique features in the photoacoustic spectrum over 100 MHz are observed. These periodically varying spectral minima and maxima depend strongly on the size, morphology, orientation, and composition of the particle (21). Quantitative analysis of the photoacoustic spectra

Submitted March 18, 2013, and accepted for publication May 20, 2013.

*Correspondence: estrohm@ryerson.ca

Editor: Denis Wirtz.

0006-3495/13/07/0059/9 $2.00

http://dx.doi.org/10.1016/j.bpj.2013.05.037

can be used to help identify these parameters and extract information from the particle examined.

The size, shape, and intrinsic optical absorption properties of RBCs make them ideal candidates for high-frequency quantitative photoacoustic methods. The photoacoustic signal can be used to infer the RBC size and shape, and thus give further insight into the specific abnormality observed than do current clinical methods. These methods could be translated into an automated device capable of measuring a large sample size for a rapid determination of RBC morphology and thus pathology.

MATERIALS AND METHODS

RBCs were extracted from a healthy male volunteer in accordance with the guidelines of the Ryerson Ethics Board (REB #2012-210). A drop of blood was drawn from the subject's finger using a lancet and immediately deposited in 1 mL Dulbecco's modified Eagle's medium (DMEM) containing 10% fetal bovine serum to maintain viability (Sigma Aldrich, St. Louis, MO). All measurements were made on 35 mm glass-bottom dishes (Mattek Corporation, Ashland, MA). The dishes were coated with a thin layer of 0.5% agar ~200 μm thick to reduce photoacoustic back reflections from the glass substrate. Approximately 30 μL of the DMEM-RBC solution was deposited into 2 mL of coupling fluid inside the glass-bottom dish to dilute the sample.

For the orientation and echinocyte measurements, DMEM was used as the coupling fluid. For the osmolality measurements, phosphate-buffered saline (PBS) was used as the coupling fluid. For both the PBS and DMEM liquids, osmolality was measured three times using a Vapro 5520 vapor pressure osmometer (Wescor, Logan, UT) and was found to be, on average, 294 and 332 mmol/kg, respectively. The standard deviation of three measurements was $\pm$10 mmol/kg. The osmolality of PBS solutions was adjusted by adding water. For the ATP-depletion procedure, the extracted blood was stored in PBS. A small sample of the PBS-RBC solution was deposited on the glass-bottom dish containing 2 mL DMEM, and 21 RBCs were measured. The PBS-RBC solution was stored at 4°C for 24 h to induce echinocyte formation, and a small sample was then added to a glass-bottom dish containing 2 mL PBS. Again, 21 RBCs were measured. Another PBS-RBC sample was added to a glass-bottom dish containing 2 mL DMEM and an additional 21 RBCs were measured. All measurements were performed at 36°C.

All measurements were completed using a photoacoustic microscope developed by Kibero (Saarbrücken, Germany). This is an Olympus IX81 inverted optical microscope fitted with a transducer above the sample stage (Fig. 1 *A*). The sample was positioned between the optical objective and the transducer. The system optics allows for viewing the sample and aligning the transducer; it also focuses the laser onto the sample. A dilute suspension of freshly extracted human RBCs was deposited into the liquid in the sample holder. Most RBCs would fall to the substrate and align horizontally, but some would initially come to rest in a vertical orientation (Fig. 1 *B*); these would eventually tip over to a horizontal orientation. The laser was focused onto single RBCs and the transducer recorded the resulting photoacoustic wave (Fig. 1 *C*). The photoacoustic signals of RBCs were measured in both a vertical and horizontal orientation. The diameter was obtained from the optical images for comparison to theoretical simulations. A transducer with a center frequency of 375 MHz and *f* number of 1 (Kibero) was used for all measurements. A 532 nm laser (Teem Photonics, Meylan, France) was focused by a 10× optical objective to an ~10 μm spot size on the sample, sufficient to irradiate a single RBC. The laser had a pulse width of 330 ps and a pulse repetition frequency of 4 kHz. Signals were amplified by a 40 dB amplifier (Miteq, Hauppage, NY), digitized at 8 GS/s using a DC252 digitizer (Agilent, Santa Clara, CA), and averaged 100–200 times to increase the signal/noise ratio. The laser power was measured at the objective using a Nova II power meter and PD10 low energy sensor (Ophir Optronics, Jerusalem, Israel). The laser power was adjusted so that the laser fluence was 20–150 mJ/cm^2 at the sample. For the orientation measurements, photoacoustic signals were recorded approximately once per second. For all other measurements, the RBC was centered over the laser spot and the photoacoustic signal was recorded. A Hamming window was applied to the measured signals, and the normalized power spectrum, $P(f)$, was then calculated using the formula

$$P(f) = 20\log_{10}\left|\frac{P_m(f)}{P_n(f)}\right|,$$

where $P_m(f)$ is the Fourier transform of the measured signal $p_m(t)$, and $P_n(f)$ is the Fourier transform of $p_n(t)$, which is the spectral response of the transducer system and electronics. This normalization signal is used to remove any artifacts due to the transducer/electronics of the system; it is generated by a 200 nm thick gold film that is spectrally flat over the transducer bandwidth, with variations of <3 dB from 100–1000 MHz. The normalization signal is typically recorded using pulse-echo ultrasound from an ultrasonically flat reflective surface (22), but the transducer bandwidth for photoacoustic measurements is larger than that for pulse-echo ultrasound. Pulse-echo ultrasound waves also travel twice the distance of photoacoustic waves emitted from the sample, and they are therefore attenuated more strongly than photoacoustic waves. More specific details about the equipment, signal processing methods, and normalization procedure can be found elsewhere (20,23).

A finite-element model (FEM) was used to validate the measured results and determine how the photoacoustic spectral features vary with different

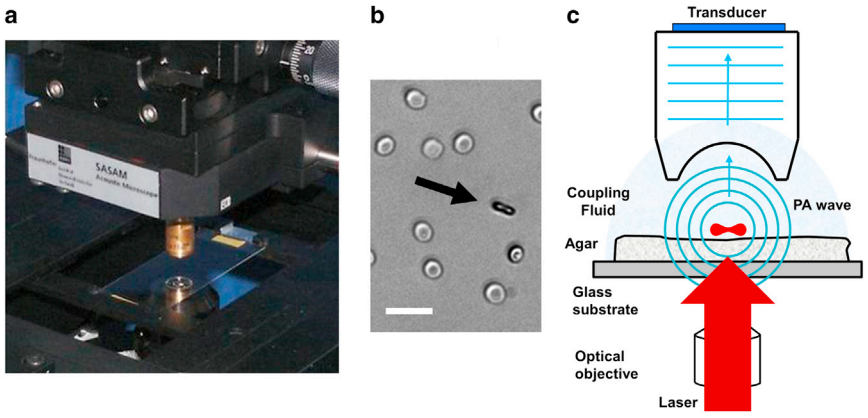

FIGURE 1 The photoacoustic microscope. (*a*) The photoacoustic microscope. The sample is positioned between the transducer and the optical objective. (*b*) RBCs after deposition into the sample holder. Most RBCs align horizontally on the substrate, but a small number align vertically (*arrow*). Scale bar, 20 μm. (*c*) A schematic showing the sample positioning relative to the transducer and focused laser. Figure 1 (*a*) used with permission from Robert Lemor at Kibero GmbH.

parameters such as the diameter and orientation. The FEM was developed using COMSOL Multiphysics software (Burlington, MA). A biconcave shape using the equation developed by Fung et al. (24) was positioned at the center of a two-dimensional axisymmetric 10 μm-radius spherical system (Fig. 2). A mesh size of 0.05 μm was used. A density of 1100 kg/m^3 (25,26) and a sound speed of 1650 m/s, similar to the sound speed measured in previous studies (27,28), were used as input parameters. The model was initiated with the RBC at a pressure higher than that of the surrounding fluid to simulate the thermoelastic expansion that occurs immediately after absorption of energy. A transient acoustics solver was used to calculate the ultrasonic pressure wave propagation from the RBC as a function of time. The signal was recorded at the system boundary at various angles around the RBC. Further details about the development of the model can be found in Strohm et al. (29).

RESULTS

Numerical simulations

Numerical simulations were performed using the FEM to compare our measurements to theoretical predictions. In these simulations, the shape of the photoacoustic spectrum was strongly dependent on the RBC size and orientation. Due to the large aspect ratio of the RBC, the photoacoustic wave generated has distinctly different spectral features depending on the relative angle of observation (Fig. 3 *A*). When a 7.82 μm RBC is oriented horizontally toward the transducer (Fig. 2, *90°*), the spectrum is essentially featureless from 100 to 500 MHz, with the first spectral minimum occurring at 800 MHz. As the RBC rotates to a vertical orientation, the spectral amplitude decreases and the spectral minimum shifts from ~800 MHz (at 90°, horizontal orientation) to 250 MHz (at 0°, vertical orientation). The RBC diameter also affects the location of the spectral minima (Fig. 3 *B*). When oriented vertically, the first spectral minimum shifts from 200 MHz (8.80 μm diameter) to 270 MHz (6.60 μm diameter).

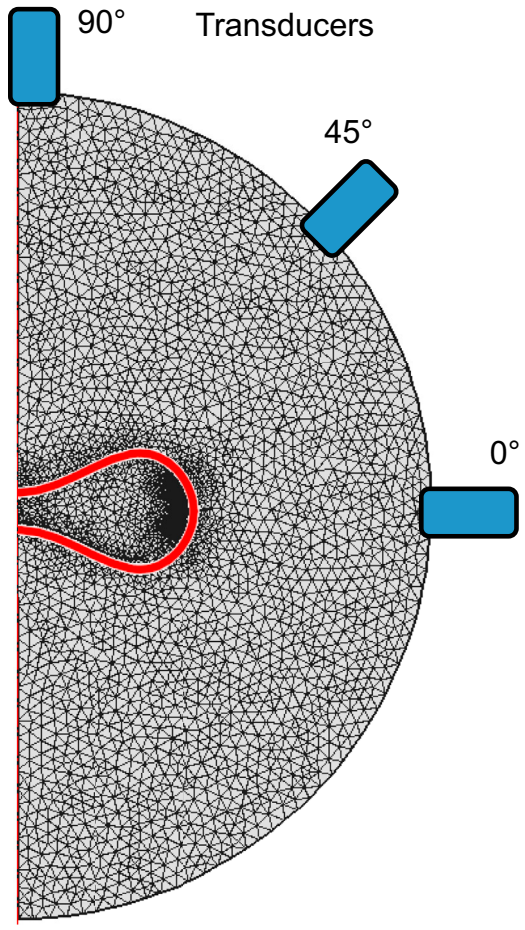

FIGURE 2 The FEM developed to describe the photoacoustic waves generated by micron-sized particles. The RBC was positioned at the center, and transducers recorded the emitted photoacoustic wave around the RBC.

Photoacoustic signals versus RBC orientation

Photoacoustic signals were recorded from a single 7.8 μm-diameter RBC, first in the vertical orientation, then in a horizontal orientation after it fell over. The time domain signal as recorded in both orientations is shown in Fig. 4 *A*. Aside from the change in signal amplitude, it is difficult to infer any details about the RBC from these signals alone. Fig. 4 *B* shows the power spectrum of the signals from Fig. 4 *A* for the same RBC. In the vertical orientation, periodically varying minima and maxima are observed throughout the spectrum, starting at 200 MHz. In the horizontal orientation, the photoacoustic spectrum is nearly flat and featureless over the bandwidth of the transducer (~150–550 MHz). Good agreement between our measurements and FEM simulations was observed for the 7.8 μm RBC oriented vertically and horizontally (Fig. 4 *B*). To examine how the signal varied with angle, an animation showing the photoacoustic time domain signal, power spectrum, and optical images of a single RBC tipping from a vertical to horizontal orientation is provided in the Supporting Material (Movie S1). A gradual increase in the frequency and amplitude of the spectral minima and maxima was observed as the RBC rotated from the vertical to the horizontal orientation, in agreement with theoretical predictions (Fig. 3 *A*).

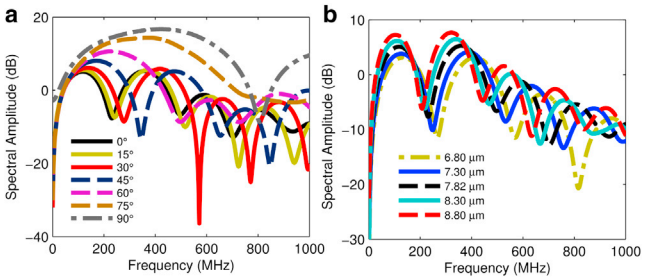

FIGURE 3 Numerical simulation results using the FEM. (*a*) The photoacoustic spectrum as the transducer position was varied from 0° (vertical RBC) to 90° (horizontal RBC) for a 7.82 μm-diameter RBC. (*b*) The photoacoustic spectrum calculated from a vertical RBC as the diameter was varied from 6.80 μm to 8.80 μm.

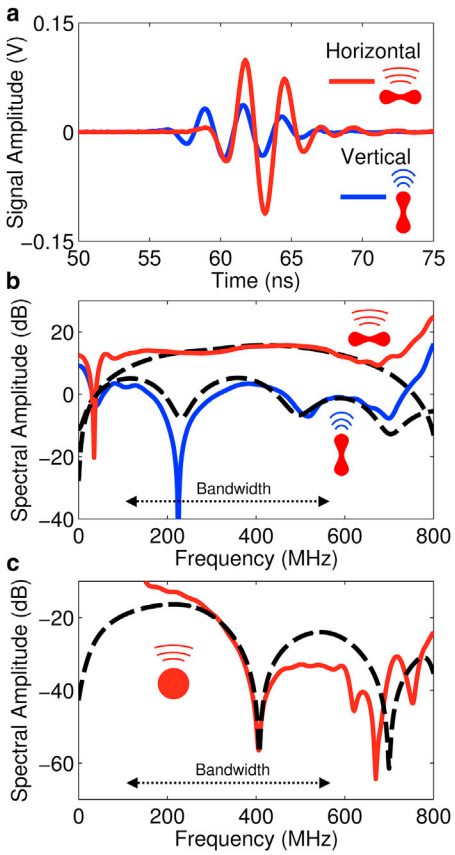

FIGURE 4 Photoacoustic measurements of single RBCs. (*a*) The time domain signal as measured from a single 7.8 μm-diameter RBC when aligned vertically (*blue*) and horizontally (*red*) relative to the transducer, measured in PBS at isotonic conditions. (*b*) The photoacoustic power spectrum of the RBCs shown in Fig. 3 *a* when aligned vertically (*blue*) and horizontally (*red*) compared to the numerical simulations for their respective orientations (*dashed black line*). (*c*) The photoacoustic spectrum of a 5.8 μm diameter RBC induced into a spherical shape by immersion in a hypotonic solution of 84 mmol/kg (solid red line) compared to numerical simulations of a spherical morphology (dashed black line). A schematic of the RBC shape and orientation is shown inset within the figure. The transducer bandwidth is from ~150 to 550 MHz as indicated by the dotted arrow. The signal amplitude has been normalized to match theory.

Photoacoustic signals versus RBC morphology

RBCs maintain their biconcave shape in isotonic conditions (~300 mmol/kg). When RBCs are immersed in a hypotonic solution, the RBC swells, with the swelling increasing as the osmolality decreases until they eventually form spherocytes (30). The photoacoustic signals from spherical RBCs were investigated by immersing healthy RBCs in a hypotonic solution of 84 mmol/kg. The diameter and spherical morphology were confirmed optically. Fig. 4 *C* shows the power spectrum of a 5.8 μm-diameter spherical RBC compared to theoretical predictions using the FEM. Regarding the location of the spectral features, good agreement was observed between measurements and theory, and these results were distinctly different from those observed for the biconcave shape in any orientation (Fig. 4 *B*).

We showed in Fig. 4 that the photoacoustic power spectrum varied depending on the RBC orientation and morphology. For an RBC aligned horizontally, the spectrum was fairly flat over the 150–550 MHz bandwidth of the transducer. In this orientation, the signal depends on the RBC thickness; for a healthy RBC, the thickness is <1 μm at the center. As an RBC swells, the thickness increases, which affects the photoacoustic signal. Fig. 5 *A* shows the average power spectrum of 21 RBCs in a horizontal orientation immersed in PBS ranging from isotonic (294 mmol/kg) to hypotonic conditions (84 mmol/kg), where the error bars indicate the standard deviation of the averaged measurements. As the osmolality decreases, the RBC swells, eventually forming a spherical shape below 120 mmol/kg. At frequencies $>$300 MHz, the spectral amplitude gradually decreases as the osmolality decreases. Below 147 mmol/kg, distinct spectral minima can be observed between 300 and 400 MHz, similar to those observed in Fig. 4 *C*. These spectral features indicate that the RBCs are becoming spherical (at 147 mmol/kg) or are spherical (84 and 118 mmol/kg), which was confirmed through optical imaging. Most of the RBCs at each osmolality exhibited similar spectra. All 21 spectra for the 294 mmol/kg (Fig. 5 *B*) and 147 mmol/kg (Fig. 5 *C*) are shown to demonstrate the consistency between measurements.

When the ATP energy stores of RBCs are depleted, the RBCs form irregularly shaped echinocytes that have spiky protrusions called spicules over the surface (31,32). This process is sometimes reversible depending on how they were formed. The photoacoustic signals from echinocytes were compared to normal RBCs. The photoacoustic power spectrum of freshly extracted human RBCs was measured in cell culture medium to determine the baseline spectrum. The RBCs were then immersed in PBS for 24 h to deplete the ATP to form echinocytes, and the photoacoustic power spectrum was measured again. Immediately afterward, the RBCs were added to cell culture medium to replenish the depleted ATP and restore the natural RBC shape. After 15 min, the photoacoustic spectrum was measured. A total of 21 RBCs were measured at each stage. Fig. 6 *A* shows the power spectrum of RBCs in these three states along with representative images. Visually, the echinocytes appeared as an irregularly shaped spiculated cell, differing from the biconcave shape or induced spheres observed previously. The average echinocyte spectrum appears to have a spectral shape similar to that of swollen RBCs in a hypotonic solution (Fig. 5 *C*, *147 mmol/kg*), where both have a minimum around 400 MHz. However, several features differentiate the swollen RBCs from echinocytes. The decrease in amplitude from the spectral maximum (~200–250 MHz) to the spectral minimum (400 MHz) was about half of what was observed, 15 dB for the echinocytes compared to 30 dB for the swelled RBCs. The echinocyte measurements also had a higher standard deviation, which can be explained by the variations in spectral shape of

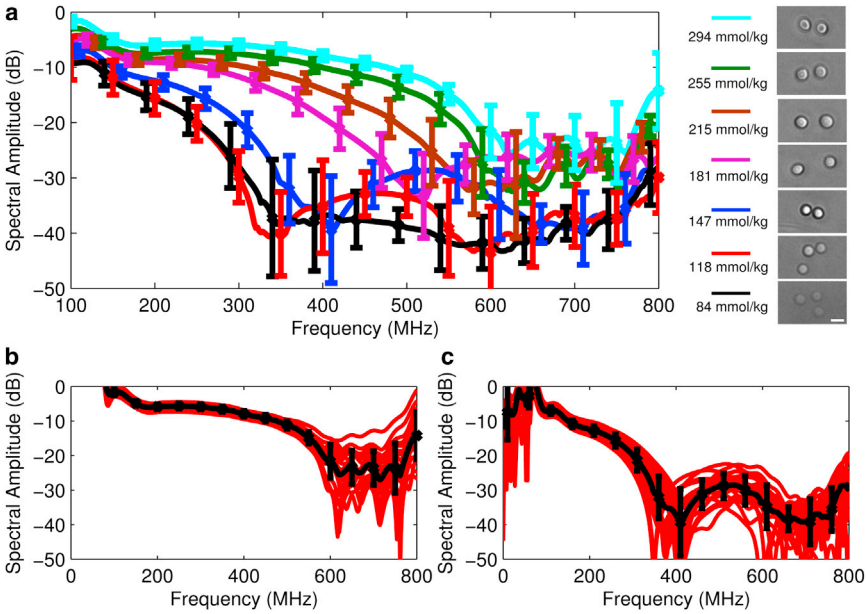

FIGURE 5 Photoacoustic spectral variations with RBC morphology. (*a*) The photoacoustic spectrum from an average of 21 RBCs measured in PBS with decreasing osmolality. Error bars indicate the mean ± SD. As the osmolality decreases, the RBCs swell, resulting in a gradual decrease of the photoacoustic spectral amplitude. Optical images confirm the change in morphology, but it is difficult to quantify the change. Scale bar, 10 μm. (*b* and *c*) The photoacoustic spectrum of each individual RBC measurement (*red*) and the average of all 21 measurements (*black*) at 294 mmol/kg (*b*) and 147 mmol/kg (*c*).

each individual RBC (Fig. 6 *B*). Furthermore, the second spectral peak that occurs around 500–600 MHz for the swollen RBCs is not present for the echinocytes. The spectral variations are likely due to the irregular shape of the echinocytes, and can be used to help differentiate the echinocyte from other morphologies. After immersion in the cell culture medium for 15 min, the RBCs rebounded back to their normal biconcave shape. The spectrum was similar to that observed before ATP depletion, with standard deviations similar to those shown in Fig. 6, where there is minimal variation between the 21 measurements (Fig. 6 *C*). Optical imaging confirmed that the RBCs had returned to their normal shape (Fig. 6 *A*, *inset*).

Quantitative spectral analysis

In our measurements, the spectral amplitude (dB) and spectral slope (dB/MHz, change in signal versus frequency) within a narrow bandwidth of the spectrum were used to quantify changes in the photoacoustic signals. The slope between 275 and 300 MHz and the amplitude at 288 MHz for the spectra in Figs. 5 (spectrum versus osmolality) and 6 (spectrum versus ATP depletion) are presented in Tables 1 and 2, respectively, where the error is given by the standard deviation between the 21 measurements. This portion of the spectrum was chosen because it occurs before the first significant minimum at 320 MHz and shows variations not

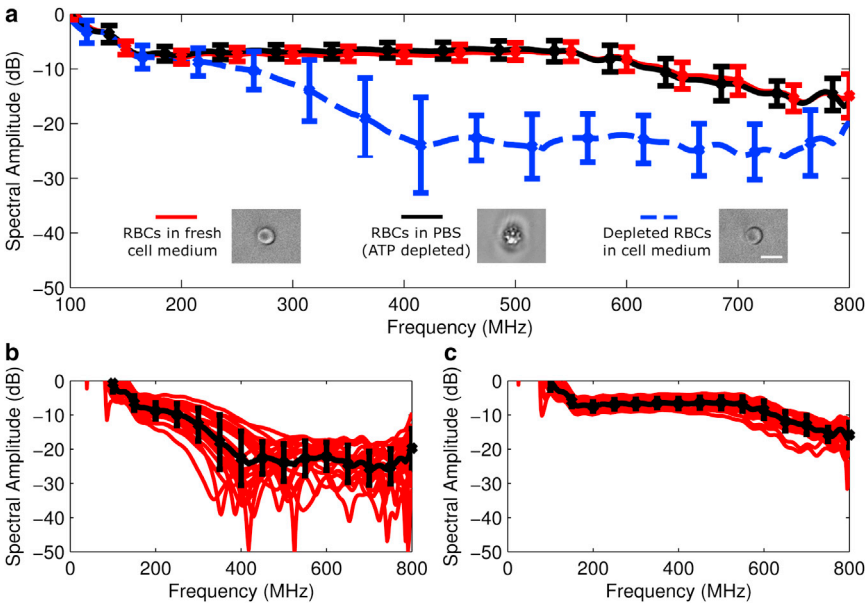

FIGURE 6 Photoacoustic spectrum of healthy RBCs and echinocytes. (*a*) The photoacoustic spectrum of RBCs in DMEM cell culture medium (*red*), left in PBS for 24 h, resulting in the formation of echinocytes (*black*), and after the echinocytes were returned to cell culture medium to restore the normal biconcave shape (*blue*). (*Inset*) Images of the RBCs at the three stages. The photoacoustic spectrum of the echinocytes is very different from that of the normal RBCs. The spectra of the RBCs in fresh medium (*red*) and the ATP-depleted RBCs in medium (*blue*) are similar, showing that the echinocytes can be restored to their normal biconcave shape. Scale bar, 10 μm. (*b* and *c*) The photoacoustic spectrum of each individual RBC measurement (*red*) and the average of all 21 measurements (*black*) of echinocytes in PBS (*b*) and subsequently in medium (*c*). A much larger variation between spectra is observed for the echinocytes compared to normal or swollen RBCs.

TABLE 1 Quantitative parameters for RBCs in PBS with varying osmolalities

Osmolality (mmol/kg)	Spectral amplitude at 288 MHz (dB)	Spectral slope at 275–300 MHz (dB/MHz)
294	−5.8 ± 0.7	−0.006 ± 0.004
255	−7.4 ± 0.9	−0.009 ± 0.004
215	−9.3 ± 1.1	−0.022 ± 0.006
181	−11.0 ± 1.1	−0.042 ± 0.012
147	−18.1 ± 2.3	−0.112 ± 0.026
118	−26.1 ± 3.7	−0.217 ± 0.073
84	−25.2 ± 5.4	−0.176 ± 0.084

Spectral amplitude and spectral slope were calculated between 275 and 300 MHz in Fig. 5 for the RBCs immersed in PBS with osmolality ranging from 294 to 84 mmol/kg. Statistically significant differences in the spectral amplitude and spectral slope were found between each change in osmolality from 294 to 118 mmol/kg ($p < 0.001$), but not between 118 and 84 mmol/kg. At these two osmolalities, the RBCs were spherical and their spectral shapes are similar.

observed at lower frequencies. A one-sided *t*-test was used to test for statistical significance between samples. A statistically significant change in the spectral slope and amplitude was observed between each change in osmolality from 294 to 118 mmol/kg ($p < 0.001$). From 118 to 84 mmol/kg, the change in spectral amplitude and spectral slope was not significant ($p > 0.05$). This was likely because the RBCs were spherical at these two osmolalities, and reducing the osmolality further had no effect. For the echinocyte data presented in Fig. 6, a significant difference ($p < 0.001$) in the spectral amplitude and slope was observed between RBCs that have been ATP depleted in PBS and either freshly extracted RBCs in medium (before ATP depletion) or echinocytes after immersion in medium (to restore the ATP). Comparing the differences between the freshly extracted RBCs in medium and echinocytes in medium (ATP was restored and the echinocytes regained their normal biconcave shape), the spectral amplitude was not statistically significant ($p > 0.05$); however, there was a small but statistically significant difference in the spectral slope ($p < 0.01$).

TABLE 2 Quantitative parameters of healthy and abnormal RBCs

RBC state	Spectral amplitude at 288 MHz (dB)	Spectral slope at 275–300 MHz (dB/MHz)
Fresh RBCs in culture medium (normal biconcave shape)	−7.4 ± 1.3	−0.011 ± 0.004
ATP-depleted RBCs in PBS (echinocytes)	−11.7 ± 4.1	−0.078 ± 0.045
ATP-depleted RBCs in culture medium (restored biconcave shape)	−6.8 ± 1.3	−0.008 ± 0.003

Spectral amplitude and spectral slope were calculated between 275 and 300 MHz in Fig. 6 for fresh RBCs in DMEM, echinocytes in PBS, and the same echinocytes redeposited in DMEM. The echinocytes were formed by immersing fresh RBCs in PBS for 24 h. After these echinocytes were immersed again in DMEM, they regained their normal biconcave shape. Statistically significant differences in the spectral amplitude and slope were observed between fresh RBCs and the echinocytes ($p < 0.001$). No statistically significant difference was observed between fresh RBCs and the depleted RBCs returned to DMEM ($p > 0.05$), but there was a small difference in the spectral slope ($p < 0.01$).

DISCUSSION

The morphology of blood cells has been studied extensively using ultrasound (33–35), but there have been limited studies using the closely related photoacoustics method. These experiments demonstrate the first quantitative analysis of any type using photoacoustic frequencies >100 MHz. The photoacoustic microscope used in this study is capable of high-resolution imaging similar to that of other photoacoustic microscopes that use lower-frequency transducers; however, unlike other photoacoustic microscopes, it can also be used for a broadband signal analysis using frequency bandwidths in the hundreds of MHz. Below 100 MHz, the photoacoustic power spectrum of cells is generally featureless and the shape or orientation of RBCs does not significantly affect the spectral shape or amplitude. As demonstrated in Figs. 3 and 4, distinct minima and maxima occur only above 100 MHz, where shifts of hundreds of MHz with amplitude variations of >10 dB occur as the RBC rotates. This is due to the large aspect ratio of the RBC. For RBCs measured vertically, our simulations have shown that the spectral minima and maxima shift to lower frequencies as the RBC diameter increases. The diameter can be determined from the spectral features if the orientation of the particle is known. Our goal is to translate this new measurement method to an automated flow system capable of measuring thousands of cells per second. However, there are several obstacles that must be overcome. For sequential scanning with the photoacoustic microscope, the RBCs naturally align horizontally on the substrate, and the RBC can be viewed during the measurements for confirmation of its orientation. When translated to a flow system, RBCs could be made to flow in a horizontal or random orientation using standing waves (36) or specific flow conditions (37,38). The analysis methods could be improved by including a second ultrasound transducer positioned at a specific angle from the first transducer. This would record the photoacoustic single from the RBC from a second position, which would provide more information related to cell orientation. Pulse-echo ultrasound measurements using the same transducers could also be combined with the photoacoustic measurements to help identify the cell orientation, as the ultrasound is sensitive to cell orientation at the frequencies used (39).

Our technique is highly sensitive to small variations in RBC morphology. A statistically significant difference ($p < 0.001$) in the spectral slope and amplitude was observed as the osmolality was decreased gradually from

294 to 118 mmol/kg. As the osmolality decreases and the RBC morphology shifts to a spherical shape, the spectral slope and amplitude decrease at each step. The spectrum was similar at 118 and 84 mmol/kg, and no statistical difference was found in the spectral amplitude or slope. This is not surprising, as the RBC is spherical at these osmolalities. This sensitivity to RBC shape variations is unequalled by any kind of existing automated method. In flow-cytometry analysis of RBCs, light-scattering methods could not detect changes in cell morphology until osmolality was below 170 mOsm/kg, at which point the RBCs have already undergone significant swelling (40). Modern efforts have used light-scattering methods to differentiate abnormal from healthy RBC morphologies, but these methods require thousands of measurements and cannot differentiate abnormality types (41). Our photoacoustic method is also capable of distinguishing the irregular echinocyte shape from other RBC morphologies. Echinocytes are generally a result of dehydration or high pH; when severely deformed, they are termed acanthocytes. Usually observed in vitro, the prevalence in vivo is associated with various diseases such as liver cirrhosis and heart disease, among others (42). The spectrum has a shape similar to that of nearly spherical RBCs, with a spectral minimum around 400 MHz (Fig. 5 *B*, *147 mmol/kg*), but the echinocytes can be differentiated through quantitative spectral analysis. From 200 to 400 MHz, the decrease in echinocyte spectral amplitude was half that of the swelled RBCs, and the standard deviation was higher. Good sensitivity to the morphological shape was observed using a sample size of just 21 RBCs. Automating the procedure to increase the counts by one or two orders of magnitude could give even better sensitivity, and we anticipate that we could also differentiate other types of RBC morphological abnormalities, such as stomatocytes (spherically indented) and those observed in malaria infection (irregular swelling) and sickle cell disease (cigar-shaped), among others.

A significant application of this methodology is in the diagnosis of blood-related diseases. Deviations from the regular biconcave shape are a significant indicator of RBC pathology, whether genetic, infectious, or simply from a chemical imbalance. For example, spherically shaped RBCs impede blood flow, resulting in anemia, fatigue, and splenomegaly (43). Aggregated RBCs could also be characterized using this system, as the photoacoustic signal changes depending on the type of aggregation (44). Using a tunable light source would allow for optical spectroscopy measurements using photoacoustics. The fact that absorption of RBCs varies with optical wavelength has been exploited to detect oxygenated/deoxygenated blood in vessels (45) and changes in oxygenation due to RBC aggregation (46). A theoretical framework has been developed recently to detect RBCs infected with malaria using photoacoustics as a function of wavelength (47).

Another significant application is in the characterization of donated blood. Blood can be stored up to 42 days, after which it becomes unsuitable for transfusion. After 7 days in storage, 23% of RBCs had abnormal shapes such as echinocytes and stomatocytes; after 42 days, this percentage increased to 77% (48). Using older blood results in decreased transport efficiency, poor circulation, and increasing time spent in hospital. The viability of blood is determined by the storage conditions and how it was prepared. Blood is perishable and demand is constant. There is extensive research devoted to improving the preservation methods by reducing the blood degradation and prolonging its shelf life. A method to rapidly characterize the blood morphology and thus determine its viability does not currently exist and would be useful for rapidly characterizing blood both for research purposes and immediately before transfusion (49).

CONCLUSION

Our experiments demonstrate that it is possible to quantify the morphology of RBCs using high-frequency photoacoustic spectral features with a very low sample size. Experimental measurements were validated with numerical simulations using a FEM. The photoacoustic spectral methods described are a first step toward an automated process for the detection of RBC abnormalities via morphological identification with good sensitivity. With some refinement, these methods could eventually be used in a clinical setting to help diagnose RBC pathology using just a single drop of blood. Application of the methods presented is not limited to characterization of RBCs; in fact, nearly any micron-sized particle has unique spectral features above 100 MHz that are strongly dependent on size, shape, and orientation, and these features can be used for particle characterization and/or identification. These methods are currently being applied to the analysis of other particles, such as biological cells and ultrasound/photoacoustic contrast agents (18,20).

SUPPORTING MATERIAL

One movie is available at http://www.biophysj.org/biophysj/supplemental/S0006-3495(13)00624-3.

The authors acknowledge helpful discussions and technical support from Eno Hysi and Arthur Worthington (Ryerson University, Toronto, Canada), Eike Weiss, Wolfgang Bost, and Robert Lemor (Kibero/Fraunhofer Institute, Saarbrücken, Germany), and Gregory Czarnota (Sunnybrook Health Sciences Center, Toronto, Canada) for scientific input. The authors thank David Dubins (University of Toronto) for his assistance in measuring the osmolality of our solutions.

E. Strohm is supported through a Natural Sciences and Engineering Research Council doctoral fellowship. This research was undertaken, in part, thanks to funding from the Natural Sciences and Engineering Research Council of Canada (216986-2012), the Canadian Institutes of Health Research (CCI 1117964), and the Canada Research Chairs Program

awarded to M. Kolios. Funding to purchase the equipment was provided by the Canada Foundation for Innovation, the Ontario Ministry of Research and Innovation, and Ryerson University.

REFERENCES

1. Wintrobe, M. M., J. P. Greer, and G. R. Lee. 2009. Wintrobe's Clinical Hematology. Lippincott Williams & Wilkins,, Philadelphia.
2. Chien, S. 1987. Red cell deformability and its relevance to blood flow. *Annu. Rev. Physiol.* 49:177–192.
3. Fung, Y. C. 1993. Biomechanics: Mechanical Properties of Living Tissues, Second Edition. Springer, New York.
4. Canham, P. B., and A. C. Burton. 1968. Distribution of size and shape in populations of normal human red cells. *Circ. Res.* 22:405–422.
5. Park, Y., M. Diez-Silva, …, S. Suresh. 2008. Refractive index maps and membrane dynamics of human red blood cells parasitized by *Plasmodium falciparum*. *Proc. Natl. Acad. Sci. USA.* 105:13730–13735.
6. Xu, M., and L. V. Wang. 2006. Photoacoustic imaging in biomedicine. *Rev. Sci. Instrum.* 77: 041101–041101–22.
7. Wang, L. V. 2009. Multiscale photoacoustic microscopy and computed tomography. *Nat. Photonics.* 3:503–509.
8. Wang, X., Y. Pang, …, L. V. Wang. 2003. Noninvasive laser-induced photoacoustic tomography for structural and functional in vivo imaging of the brain. *Nat. Biotechnol.* 21:803–806.
9. Wang, L. V., and S. Hu. 2012. Photoacoustic tomography: in vivo imaging from organelles to organs. *Science.* 335:1458–1462.
10. Zhang, H. F., K. Maslov, …, L. V. Wang. 2006. Functional photoacoustic microscopy for high-resolution and noninvasive in vivo imaging. *Nat. Biotechnol.* 24:848–851.
11. Kolkman, R. G. M., E. Hondebrink, …, F. F. M. de Mul. 2003. In vivo photoacoustic imaging of blood vessels using an extreme-narrow aperture sensor. *IEEE J. Sel. Top. Quantum Electron.* 9:343–346.
12. Beard, P. 2011. Biomedical photoacoustic imaging. *Interface Focus.* 1:602–631.
13. Ku, G., K. Maslov, …, L. V. Wang. 2010. Photoacoustic microscopy with 2-microm transverse resolution. *J. Biomed. Opt.* 15:021302.
14. Zhang, C., K. Maslov, and L. V. Wang. 2010. Subwavelength-resolution label-free photoacoustic microscopy of optical absorption in vivo. *Opt. Lett.* 35:3195–3197.
15. Maslov, K., H. F. Zhang, …, L. V. Wang. 2008. Optical-resolution photoacoustic microscopy for in vivo imaging of single capillaries. *Opt. Lett.* 33:929–931.
16. Yao, D.-K., R. Chen, …, L. V. Wang. 2012. Optimal ultraviolet wavelength for in vivo photoacoustic imaging of cell nuclei. *J. Biomed. Opt.* 17:056004–056007.
17. Bost, W., F. Stracke, …, R. Lemor. 2009. Developing a high-resolution photoacoustic microscopy platform. *Proc. 4th Eur. Conf. Int. Fed. Med. Biol. Eng.* 22:448–451.
18. Strohm, E. M., M. Rui, …, M. Kolios. 2011. Vaporization of perfluorocarbon droplets using optical irradiation. *Biomed. Opt. Express.* 2:1432–1442.
19. Rui, M., S. Narashimhan, …, M. C. Kolios. 2010. Gigahertz optoacoustic imaging for cellular imaging. *Proc. SPIE.* 7564:756411.
20. Strohm, E. M., I. Gorelikov, …, M. C. Kolios. 2012. Acoustic and photoacoustic characterization of micron-sized perfluorocarbon emulsions. *J. Biomed. Opt.* 17:96016.
21. Diebold, G. J., M. I. Khan, and S. M. Park. 1990. Photoacoustic "signatures" of particulate matter: optical production of acoustic monopole radiation. *Science.* 250:101–104.
22. Baddour, R. E., M. D. Sherar, …, M. C. Kolios. 2005. High-frequency ultrasound scattering from microspheres and single cells. *J. Acoust. Soc. Am.* 117:934–943.
23. Strohm, E. M., G. J. Czarnota, and M. C. Kolios. 2010. Quantitative measurements of apoptotic cell properties using acoustic microscopy. *IEEE Trans. Ultrason. Ferroelectr. Freq. Control.* 57:2293–2304.
24. Evans, E., and Y.-C. Fung. 1972. Improved measurements of the erythrocyte geometry. *Microvasc. Res.* 4:335–347.
25. Grover, W. H., A. K. Bryan, …, S. R. Manalis. 2011. Measuring single-cell density. *Proc. Natl. Acad. Sci. USA.* 108:10992–10996.
26. Godin, M., A. K. Bryan, …, S. R. Manalis. 2007. Measuring the mass, density, and size of particles and cells using a suspended microchannel resonator. *Appl. Phys. Lett.* 91: 123121–123121–3.
27. Dukhin, A. S., P. J. Goetz, and T. G. M. van de Ven. 2006. Ultrasonic characterization of proteins and blood cells. *Colloids Surf. B Biointerfaces.* 53:121–126.
28. Mohamed, E. T. A., A. E. Kamanyi, …, W. Grill. 2012. Age-dependent acoustic and microelastic properties of red blood cells determined by vector contrast acoustic microscopy. *Microsc. Microanal.* 18:436–444.
29. Strohm, E. M., E. Hysi, and M. C. Kolios. 2012. Photoacoustic measurements of single red blood cells. *Proc. IEEE Int. Ultrasonics Symp. Dresden.* 1406–1409.
30. Canham, P. B. 1970. The minimum energy of bending as a possible explanation of the biconcave shape of the human red blood cell. *J. Theor. Biol.* 26:61–81.
31. Reinhart, W. H., and S. Chien. 1986. Red cell rheology in stomatocyte-echinocyte transformation: roles of cell geometry and cell shape. *Blood.* 67:1110–1118.
32. Gov, N. S., and S. A. Safran. 2005. Red blood cell membrane fluctuations and shape controlled by ATP-induced cytoskeletal defects. *Biophys. J.* 88:1859–1874.
33. Shung, K. K., R. A. Sigelmann, and J. M. Reid. 1976. Scattering of ultrasound by blood. *IEEE Trans. Biomed. Eng.* 23:460–467.
34. Cloutier, G., and Z. Qin. 1997. Ultrasound backscattering from non-aggregating and aggregating erythrocytes—a review. *Biorheology.* 34:443–470.
35. Fontaine, I., M. Bertrand, and G. Cloutier. 1999. A system-based approach to modeling the ultrasound signal backscattered by red blood cells. *Biophys. J.* 77:2387–2399.
36. Coakley, W. T., D. W. Bardsley, …, D. J. Clarke. 1989. Cell manipulation in ultrasonic standing wave fields. *J. Chem. Technol. Biotechnol.* 44:43–62.
37. Kachel, V., E. Kordwig, and E. Glossner. 1977. Uniform lateral orientation, caused by flow forces, of flat particles in flow-through systems. *J. Histochem. Cytochem.* 25:774–780.
38. Dupire, J., M. Socol, and A. Viallat. 2012. Full dynamics of a red blood cell in shear flow. *Proc. Natl. Acad. Sci. USA.* 109:20808–20813.
39. Baddour, R. E. 2004. High frequency ultrasound scattering from microspheres and single cells [microform]. Thesis (M.Sc.), University of Toronto, Toronto.
40. Gutowski, K. A., J. L. Hudson, and D. Aminoff. 1991. Flow cytometric analysis of human erythrocytes: I. Probed with lectins and immunoglobulins. *Exp. Gerontol.* 26:315–326.
41. Piagnerelli, M., K. Zouaoui Boudjeltia, …, M. Vanhaeverbeek. 2007. Assessment of erythrocyte shape by flow cytometry techniques. *J. Clin. Pathol.* 60:549–554.
42. Brecher, G., and M. Bessis. 1972. Present status of spiculed red cells and their relationship to the discocyte-echinocyte transformation: a critical review. *Blood.* 40:333–344.
43. Perrotta, S., P. G. Gallagher, and N. Mohandas. 2008. Hereditary spherocytosis. *Lancet.* 372:1411–1426.

44. Hysi, E., R. K. Saha, and M. C. Kolios. 2012. On the use of photoacoustics to detect red blood cell aggregation. *Biomed. Opt. Express.* 3:2326–2338.

45. Zhang, H. F., K. Maslov, …, L. V. Wang. 2007. Imaging of hemoglobin oxygen saturation variations in single vessels in vivo using photoacoustic microscopy. *Appl. Phys. Lett.* 90:053901.

46. Hysi, E., R. K. Saha, and M. C. Kolios. 2012. Photoacoustic ultrasound spectroscopy for assessing red blood cell aggregation and oxygenation. *J. Biomed. Opt.* 17:125006.

47. Saha, R. K., S. Karmakar, and M. Roy. 2012. Computational investigation on the photoacoustics of malaria infected red blood cells. *PLoS ONE.* 7:e51774.

48. Blasi, B., A. D'Alessandro, …, L. Zolla. 2012. Red blood cell storage and cell morphology. *Transfus. Med.* 22:90–96.

49. Scott, K. L., J. Lecak, and J. P. Acker. 2005. Biopreservation of red blood cells: past, present, and future. *Transfus. Med. Rev.* 19:127–142.